Seeds of imperfection rule the
mesocrystalline disorder in natural anhydrite single crystals

Tomasz M. Stawski*[1], Glen J. Smales[1], Ernesto Scoppola[2], Diwaker Jha[3],
Luiz F. G. Morales[4,5], Alicia Moya[6], Richard Wirth[7], Brian R. Pauw[1], Franziska Emmerling[1, 8],
and Alexander E. S. Van Driessche**[6]

* tomasz.stawski@bam.de; **Alexander.Van-Driessche@univ-grenoble-alpes.fr

1. Federal Institute for Materials Research and Testing (BAM), 12489, Berlin, Germany;
2. Max Planck Institute of Colloids and Interfaces, 14476 Potsdam, Germany;
3. HyperSpecs GmbH, Berlin, Germany
4. Scientific Center for Optical and Electron Microscopy (ScopeM), ETH Zürich, 8093, Zürich;
5. Geological Institute, Department of Earth Sciences, ETH Zürich, 8092 Zurich, Switzerland;
6. Université Grenoble Alpes, Université Savoie Mont Blanc, CNRS, IRD, IFSTTAR, ISTerre, F-38000 Grenoble, France;
7. German Research Centre for Geosciences, GFZ, Interface Geochemistry, Telegrafenberg, 14473 Potsdam, Germany;
8. Humboldt-Universität zu Berlin, Department of Chemistry, 12489, Berlin, Germany

Orcid:
TMS: https://orcid.org/0000-0002-0881-5808
GJS: https://orcid.org/0000-0002-8654-9867
ES: https://orcid.org/0000-0002-6390-052X
DJ:
LFGM: https://orcid.org/0000-0002-8352-850X
AM: https://orcid.org/0000-0002-0328-012X
RW:
BRP: https://orcid.org/0000-0002-8605-838X
FE: https://orcid.org/0000-0001-8528-0301
AESVD: https://orcid.org/0000-0003-2528-3425

Keywords:
Calcium sulfate; anhydrite; Naica; single crystal; crystallisation; nucleation; particle-mediated

Competing Interest Statement:
The authors declare no competing interest.

Significance statement

In a popular view, many perceive crystals as the embodiment of perfect order, a belief that has led to ascribe near mystical powers to those objects. In reality, it is scientifically well-understood that monocrystals must be imperfect and contain at least around-atomic-scale point, line or planar defects. By considering large anhydrite crystals from the famous Naica "cave of crystals", a new extended picture emerges, revealing a suite of correlated self-similar void defects spanning across many length-scales. These flaws in the macroscopic crystal likely stem from disorder introduced by "seeds of imperfection" originating from a particle-mediated nucleation pathway. Thus, the building of a crystal could be viewed as nature failing to fill rows in Tetris, a game one will never truly win.

Abstract

In recent years, we have come to appreciate the astounding intricacy of the formation process of minerals from ions in aqueous solutions. In this context, a number of studies have revealed that nucleation in the calcium sulfate system is non-classical, involving the aggregation and reorganization of nanosized prenucleation particles. In a recent work we have shown that this particle-mediated nucleation pathway is actually imprinted in the resultant single micron-sized $CaSO_4$ crystals. This property of $CaSO_4$ minerals provides us with an unique opportunity to search for evidence of non-classical nucleation pathways in geological environments. In particular, we focused on the quintessential single crystals of anhydrite extracted from the Naica mine in Mexico. We elucidated the growth history from this mineral sample by mapping growth defects at different length scales. Based on these data we argue that the nano-scale misalignment of the structural sub-units observed in the initial calcium sulfate crystal seed propagate through different length-scales both in morphological, as well as stictly crystallographic aspects, eventually causing the formation of large mesostructured single crystals of anhydrite. Hence, the nanoparticle mediated nucleation mechanism introduces a "seed of imperfection", which leads to a macroscopic single crystal, in which its fragments do not fit together at different length-scales in a self-similar manner. Consequently, anisotropic voids of various sizes are formed with very well-defined walls/edges. But, at the same time the material retains its essential single crystal nature. These findings shed new light on the longstanding concept of crystal structure.

Introduction

The formation, transformation and dissolution of minerals in aqueous solutions plays a key role in the natural and engineering evolution of the Earth's surface. They control geological processes as diverse as the mass transfers within the lithosphere, elemental cycling, natural water composition, soil formation and biomineralization in living organisms, sequestration of CO_2, (sea)water desalination, geological nuclear waste storage, the setting of cement, and the synthesis of advanced functional materials, to name just a few. Although there are long standing theories to explain these mineral processes, in recent times a vast amount of new evidence has surfaced challenging these traditional views. In the particular case of nucleation, a number of precursor and intermediate solute/solid species, both stable and metastable, have been identified. The observation of these prenucleation phases extends the classical view of one step nucleation towards multi-step "non-classical" models[1–3].

Although these recent insights have significantly expanded our view of mineral formation, only a reduced matrix of physicochemical parameters have been explored in the lab, which may not be (fully) representative of conditions prevalent in natural or even engineered environments. Consequently, it remains uncertain whether the observed multistep pathways in the laboratory setting are truly universal or only incidental.

To evaluate the general applicability of these so-called "non-classical" mechanisms to out-of-the lab environments, mineral formation should ideally be observed in situ. Nevertheless, this is a daunting task taking into account the inherent stochastic nature of the nucleation process, combined with the close to equilibrium conditions usually prevailing in natural environments. One way to circumvent these difficulties is to identify evidence/remnants of the non-classical nucleation pathways within the final crystals, similar to what has been reported for several biominerals[4]. Recently, we have revealed that the particle-mediated nucleation pathway of $CaSO_4$ [5–7] is imprinted in the resultant single crystals[8], which are almost universally mesocrystalline[9–11] in nature. This property of calcium sulfate minerals provides us with a unique tool to search for evidence of non-classical nucleation pathways in different geological processes spanning time-scales of 1000s of years and beyond[12]. In particular, we focused on single crystals of natural anhydrite (i.e. anhydrite AII phase). Together with gypsum, anhydrite is commonly encountered in evaporitic, and also hydrothermal, environments on the Earth's surface[7]. Although there are different polymorphs[13–15] (AI,AII and AIII; see SI: Supplementary Note 1 and Fig. S1), only anhydrite AII crystallizes from aqueous solutions[16–18], either directly or via a dissolution and reprecipitation process from gypsum. In the Naica Mine in Mexico (Cave of the Crystals or Giant Crystal Cave or Cueva de los cristales), anhydrite samples exceeding 10 cm in length[19–21] (see SI: Figs. S2 and S3) can be found and these large natural crystals of anhydrite AII contain a unique register of nanometers to macroscopic length-scales growth processes taking place over a period of millenia.

We used a multitechnique approach to extract the growth history of an anhydrite single crystal from the Naica mine to better understand its internal structure at different length scales and correlate it with the particle-mediated crystallization model of calcium sulfate[22–24]. In particular, we argue that the nano-scale misalignment of the structural sub-units observed in the initial calcium sulfate crystal seed propagate through different length-scales both in morphological, as well as strictly structural aspects, eventually causing the formation of large mesostructured single crystals of anhydrite.

Results

Heterogeneities observed in "single" anhydrite crystals with electron microscopy

Fig. 1 shows HRTEM lattice fringe images of two FIB foils obtained from arbitrary locations several μm apart from each other of a single anhydrite crystal, (Figs. 1A&B). Both images display the same crystal orientation and their near-identical FFTs, showing only individual maxima (FFT-calculated diffraction spots), which confirms that the material is indeed single crystalline in nature (inset I in Fig. 1A and II in Fig. 1B). The relatively long distance (several μm) between both fields of view, further indicates that we are dealing with a continuous single crystal, which is in agreement with X-ray diffraction measurements. However, the individual spots in the FFTs are not circular in shape but instead elliptical. This directly implies mosaicity at the length-scales corresponding to the field of view of the HRTEM images. To emphasize any structural variations we used Fourier filtering [8] to calculate the

inverse FFT real-spaces images corresponding to the HRTEM micrographs (Figs. 1C&D). In addition, a fake-colour map was applied to highlight the structural features. The obtained images indicate that the HRTEM regions shown in Fig. 1A and B are composed of areas with lattice fringes aligned in the same manner (areas marked with pink rectangles in complementary representations in Fig. 1). However, the extent of order within the crystal lattice continuously fluctuates, with better ordered domains separated by less ordered ones. If we trace selected fringes across the field of view (straight lines in Fig. 1C), it becomes apparent that some domains are slightly misaligned by <1° (see arrows in inset III in Fig. 1C). Small amorphous and/or disordered areas act as transitional parts between the ordered areas (see arrows in inset IV in Fig. 1D). Based on HRTEM, these order-disorder structural modulations occur typically at a length-scale of ~10-20 nm.

We also collected SAED patterns from the FIB foils using an effective aperture of ~1 µm (SI: Fig. S4). The obtained data confirm the single crystalline nature of the anhydrite specimen, while the elliptical diffraction spots indicate strong mosaicity in the [0 1 0] direction. This indicates that the observed order-disorder regions are anisotropic, with shorter length-scales perpendicular to [0 1 0] and longer-ones parallel. This is also directly visible in real-space (Fig. 1), but the HRTEM images represent significantly smaller areas of the crystal than the one from which the SAED was obtained. Therefore, the latter indicates that the alignment of the anisotropic defects extends over a length-scale of at least 1 µm. Noteworthy, the SAED also contains a significant (i.e. above noise) diffuse scattering contribution, i.e. a raster of streaks parallel to the [1 0 0] and [0 1 0] directions and passing through the diffraction spots. Fig. S4 in SI shows that scattering in the [0 1 0] direction has higher intensity than the one in the [100] direction. Although it might be difficult to unequivocally interpret the origin of the diffuse scattering without in-depth structural modelling [25–30], it appears reasonable to conclude that the observed streaks are related to the presence of the aforementioned order-disorder modulation regions (Fig. 1). These regions are most likely arranged into planes or rods with their long axis oriented in plane with respect to the field view.

Finally, it should be noted that FIB-prepared TEM lamellae may have up to 30 nm of amorphous material on both sides [31–34]. With a sample thickness of approximately 150 nm the scattering volume of the undisturbed crystal is substantially larger than the amorphous or FIB affected layer on both sides of the foil. Furthermore, this effect should reveal itself as a decrease in the diffraction contrast because the amorphous layer is perpendicular to the beam during the TEM imaging [34]. Conversely, in our thin sections the order-disorder modulation is parallel to the beam, since we observe in transmission, which indicates that it is highly unlikely to be a result of the FIB thinning. Furthermore, the observed structural effects correlate with the results from other techniques as we show further.

Structural heterogeneity in X-ray scattering from a single anhydrite crystal
The internal homogeneity of an anhydrite single crystal was also probed by means of transmission X-ray scattering measurements at scattering vector q-ranges corresponding to SAXS (~1-70 nm) and WAXS (<1 nm). In contrast to HRTEM, the signal measured by scattering originates from a large sample volume, ~1 mm^3. The general considerations on how an idealised single crystal ought to scatter in SAXS and WAXS are summarised in SI: Supplementary Note 2. Fig. 2 presents 2D SAXS patterns for an anhydrite crystal in position S at 0° and 21° tilt respectively (see also SI: Fig. S3). For either of the two crystal orientations, distinctly different anisotropic scattering patterns are observed. The patterns

show that the anhydrite crystal structure is heterogeneous at the length-scale of < ~70 nm (Q_{min} > 0.1 nm^{-1}), and that these structural heterogeneities are orientated. The fact that we can observe such structural features in the first place means that their average electron density is different from the one of the surrounding matrix. It can be either higher, which is unlikely since anhydrite is the densest phase of $CaSO_4$, or lower if they are amorphous and/or constitute empty voids/pores. In Fig. 2A, the direction of the high-intensity scattering pattern is parallel to the apparent vertical long axis of the crystal (inset in Fig. 2A). This suggests that the nanosized structural features from which this pattern originates have their shorter dimensions aligned perpendicularly to the crystal vertical long axis (and thus their longer dimensions parallel to the long axis). When the crystal is tilted the resulting cross-shaped scattering patterns represent cross-sectional components of the elongated objects. The obtained cross-sections present a more complex scattering pattern (Fig. 2B). The intensity in Fig. 2B extends to lower-Q than the one in Fig. 2A (compare Q_x and Q_y scales). Hence, scattering in Fig. 2B originates from larger scattering features, than the one in Fig. 2A. Such a cross-shaped pattern for the tilted orientation together with the one from Fig. 2A implies that the scattering objects are rod-like or platelet-like in nature, with the long-axis of the objects aligned parallel to the long axis of the crystal. Furthermore, the scattering profile in the direction perpendicular to the long axis of the crystal exhibits small-angle diffraction peaks (indicated with arrows in Fig. 2B). Such peaks most likely originate from a regular arrangement of mesoscale features in the crystal along this direction. A more complete interpretation is presented further in the text in the context of the microtomography data.

In order to compare intensities, 2D patterns were converted to polar coordinates (SI: Fig. S5A&B), based on which we calculated 1D scattering profiles (see SI: Supplementary Note 3) from the selected directions (dotted lines in Figs. 2A&B). The resulting 1D scattering profiles in Fig. 2C have the form of straight lines in a log-log representation, with both converging to background scattering at ~1000 cts. Both profiles scale proportionally to $I(Q) \propto Q^{<-3}$, but the exponents are higher than the typical smooth interface dependence of $I(Q) \propto Q^{-4}$ (Porod interface [35,36]). These relatively feature-poor forms indicate that scattering arises from objects extending beyond the available Q-range and/or exhibit high polydispersity, indicating that the objects are >~70 nm. In addition, the scattering exponents between <-3 and >-4 point to rough interfacial, surface-fractal-like scattering [37], but due to the limited Q-range this cannot be unequivocally confirmed. The high-intensity profile (black curve, Fig. 2C) converges to background scattering at Q of ~1 nm^{-1}, whereas the low-intensity scattering (purple curve, Fig. 2C) converges at ~0.3 nm^{-1}. This implies that the length-scale aspect ratio between the perpendicular scattering features is >3:1. For the tilted orientation, shown in Fig. 2D, the perpendicular scattering patterns (I & II) are similar in terms of intensity and the characteristic length-scales. In both cases the dominant interfacial scattering exponent is <-3 and the patterns converge to the background level at ~0.6 nm^{-1}. However, scattering profiles in II, in addition to an interfacial-type scattering profile (i.e. a straight line), also exhibit relatively well-pronounced small-angle diffraction peaks corresponding to d-spacings of 22, 19, 13 and 12 nm. Profile III in Fig. 2D is calculated from a "streak" in Fig. 2B in direction 0° (see also SI: Fig. S5B and Supplementary Note 3) and contains a straight-line interfacial component, but its scaling follows a less steep dependence of $I(Q) \propto Q^{-2.5}$, and small-angle diffraction peaks at 13, 9 and 7 nm. The presence of peaks in II and III indicate the contribution of a scattering structure factor $S(Q)$,

which describes the regular arrangement of the scattering objects. The occurrence of such a structure factor has two major implications: (1) it potentially explains why the observed interfacial scattering exponents are less steep than the expected -4; (2) $S(Q)$ is direction-dependent and the contributing scattering features are closely-spaced/correlated only along the directions where the peaks are observed.

In summary, the SAXS data tell us that (1) the single crystal is structurally heterogeneous at the mesoscale; (2) the heterogeneities are highly anisotropic and preferentially orientated, where their longer dimensions parallel to the apparent long axis of the crystal; (3) the tilt of the crystal reveals the presence of a paracrystalline structure factor only in some cross-sectional directions. Although the exact crystallographic alignment of $S(Q)$ with respect to the crystal structure is not known, its presence could be explained by the fact that the anisotropic scattering features are, to a certain degree, regularly arranged in the plane perpendicular to the long axis, where the actual scattering profiles with peaks (II and III in Fig. 2D) originate from cross-sections (between 0 and 90°) of such anisotropic superstructure.

Fig. 3A shows a four-panel composite WAXS diffraction pattern in polar coordinates from an anhydrite crystal at 0° relative tilt. The patterns were measured for four orientations (SI: Fig. S3B) resulting from a rotation of the crystal around the goniometer's vertical axis, Z. Consecutive panels correspond to positions: S (starting), N (180° clockwise), W (90° clockwise), E (270° clockwise). The pattern comprises individual diffraction spots, which confirms again that we deal with a single-crystalline material. The diffraction spots are in general very similar in shape and broadening, and at first glance they do not reveal any obvious structural defects, such as strong mosaicity. However, in our WAXS measurements, we probed only a very limited set of crystal orientations. Furthermore, there are some very apparent exceptions from this trend, most noticeable for the peaks at Q ~28 nm^{-1} (marked with arrows in Fig. 3A). The strongest among those reflections is at 166° in panel S, and has the form of a cross (dashed white rectangle in Fig. 3A). The reflection appears to be broadened both in Q- and azimuthal-angle directions, and in addition composed of several sub-reflections (Fig. 3B). This cross also has an asymmetric counterpart for the same Q at 76° in the same panel (i.e. 90° apart in the azimuthal angle), and weaker analogs at 5° and -85° in panel N, due to the rotation of a crystal by 180° around the Z-axis (SI: Fig. S3B). The reflections in panel S are also accompanied by long streak lines extending at 90° in directions parallel to the cross in Cartesian coordinates (Fig. 3C), which makes them appear as curves in polar coordinates (Fig. 3B). For a given peak the two considered broadening values in polar coordinates are essentially independent from each other, because they are related to different structural effects. The increased broadening in the Q-direction is correlated with structural effects, which typically affect the lattice d-spacing e.g. caused by strain. The broadening in the azimuthal direction expresses the structural coherence of a crystal and is a measure of mosaicity, as is the case for the reflections at Q ~ 28 nm^{-1}. The observed occurrence of such mosaic effects only for a single group of diffraction spots implies that the potential defects in the crystal structure are strongly anisotropic. Furthermore, the observed streaks are indicative of diffuse scattering, which implies the presence of anisotropic amorphous features at the mesoscale associated with the structural defects. Both effects (strong mosaicity and diffuse scattering) are in agreement with the earlier interpretation of the SAXS patterns and TEM data.

X-ray microtomography (μCT)

We further evaluated the structure of a single crystal at the micrometer-length scale using X-ray μCT. This technique allows for 3D visualisation of a structure based on the absorption contrast i.e. differences in electron density at a resolution of 550x550x550 nm^3 voxel-size. In Fig. 4A two selected 3D projections of a reconstructed crystal derived from ring-uncorrected slices are shown (see Methods). These images reveal the presence of voids within the crystal volume. In SI: Videos S1 and S2 complete 360° rotations of the crystal are shown: around the Z-axis in the XY-plane, and around Y in the XZ-plane, respectively. These renderings show that the crystal volume contains objects of different sizes, spanning from several tens of microns down to objects at the voxel-size resolution limit. Fig. 4B shows two of the ring-corrected and cropped XY slices of the crystal (Z direction is in plane), which contain a number of these objects (in blue), surrounded by a relatively homogenous matrix (in brown). Considering the origin of contrast in μCT, the objects have significantly lower absorption than the surrounding crystal matrix, and are thus voids/pores within the crystal. These voids exhibit very straight and well-defined edges in the XY-plane (as indicated by the intensity profile function in the inset in Fig. 4B). A selected projection of a segmentation highlighting the voids is presented in Fig. 4C, and in addition SI: Video S3 contains a full-rotation of these objects around the Z-axis in the XY-plane. Overall, voids are clustered into channel-like features parallel to the Z-axis (long-axis) of the crystal. Along Z, the largest (~25 μm in XY) of those form continuous regular structures, whereas the smaller ones, although not necessarily connected with each other, are still grouped into pillar-like arrangements. To further evaluate the properties of the void arrangements we performed statistical analysis on all the slices (Fig. 4D, see Methods for details). This analysis highlights what is directly observable in Fig. 4C, and in SI: Video S3., i.e. on average the features are anisotropic, with a width <~5 μm and a length >~10 μm in XY, and <~5 μm for width and >~5 μm for length in YZ. In addition, they exhibit preferred orientation in the Y direction of the XY-plane (at 90° to X, hence parallel to Y), and in the Z-direction in the ZY-plane (at 0° to Z, hence normal to Y), as can be seen in Fig. 4E.

Atomic Force Microscopy imaging of nano to mesoscale void structures

We further characterised the voids exposed at the crystal facets using AFM (Fig. 5). Detailed observation of different crystallographic faces revealed that on the top face (Fig. 5A) nano- to macroscopic sized porosity is present (Figs. 5B&C), while on the side faces (Fig. 5A) no such porosity is found (Fig. 5D). These multi-scale surface imaging reveals that surface voids are rectangular in shape and in the size range of nano- to micrometers (~50 nm to 25 μm). Although, with AFM the depth of these pores cannot be probed, the obtained surface images directly complement the observations made at different length scales by SAXS and μCT. A quantitative analysis of the topographical AFM images provides further information about the porosity and reveals a porosity of 7.4 ± 1.6 %, obtained as the area of the pores divided by the total area of the AFM images. Furthermore, we measured the dimensions of the pores directly from the height profiles of a wide range of AFM images (from 1 to 120 μm field-of-view), which were acquired at different locations of the same sample. Fig. 5E shows the as-obtained pore/void size distribution, which covers a wide range of pore sizes up to ~60 μm. However, pores larger than 10 μm only constitute a minor contribution to the total porosity. In fact, the highest contribution corresponds to the pores smaller than 0.5 μm. The

pore size distribution at the nanoscale highlights that a dominant pore size exists at ~85 nm as shown in Fig. 5F.

Crystallographic heterogeneity in electron backscatter diffraction
Electron backscatter diffraction measurements bridge length scales between X-ray scattering and microtomography and provide crystallographic and lattice distortion information of the studied single crystal. In Fig. 6A we show an EBSD orientation map of one of the crystal facets of the studied single crystal. This map represents an area of 51 x 51 μm^2, has a *quasi*-uniform cyan color and corroborates the idea that, at the macroscale, the studied sample is a single crystal. Crystallographic orientation plots indicate that the EBSD mapped facet is parallel to the crystal plane (9 5 3) of anhydrite. However, when we calculate the kernel average misorientation assuming a maximum misorientation of 2.5°, it becomes apparent that the probed area is composed of heterogeneous regions (Fig. 6B). This is further evidenced by low angle grain boundaries, many of them completely closed and look like small "cells" that are neighboured by other small cells that have very small mismatch angle between each other down to the resolution of 100 nm used in the map (Fig. 6C). The degree of their misorientation is very small, as seen in the histogram of Fig. 6D and on average the blue-to-green regions range from 0.3° to <1° mismatch, which is in agreement with the TEM data. The mean misorientation is 0.35° with a standard deviation of 0.22°. Furthermore, the observed misorientation does not have a random character. In Figs. 6B&D one can observe that the upper half of the image (mean misorientation 0.40°, std. dev. 0.26°) contains more pronounced disorder than the lower half (mean 0.30°, std. dev. 0.15°).

Discussion
The results presented above, render a coherent image of the meso- to microstructure of a single crystal. In general, the diffraction measurements, as well as the external appearance of the investigated mineral sample, all indicate that we are dealing with a high-quality monocrystal, whose structure can be solved using standard methods of single crystal X-ray diffraction. Nevertheless, detailed characterisation at different length-scales indicates that the anhydrite crystal contains numerous types of intercorrelated structural defects, and is overall mesocrystalline in nature. At the meso-scale i.e. <~100 nm, the local HRTEM imaging reveals that the crystal exhibits order-disorder modulation with crystallographic domains 10-20 nm in size. This modulation exhibits smooth transitions among the neighbouring regions, and is best interpreted as a reminiscence of the particle mediated crystallization, as we explain below. The tiny mis-alignments (<1º) at the mesoscale in combination with the disordered/amorphous regions constitute a "seed of imperfection" as the crystal grows, resulting in the formation of a mesocrystal, as seen in SAED or WAXS. Our earlier studies [5,6,38] on the nucleation and growth of gypsum and bassanite, as well as those conducted by other groups [39–45], show that the crystalline phases of $CaSO_4$ nucleate within a micron-sized amorphous matrix, of aggregated primary species, several nanometers in size (for gypsum sub-3 nm) during the course of dehydration. In this regard, the selection of the actual crystalline phase is dictated by thermodynamic conditions of the chemical environment, and the amorphous aggregates may constitute a structurally universal precursor phase preceding all three phases of $CaSO_4$ [7]. Importantly, the miniscule misorientations of the order of <1° observed here, were also reported for other systems (e.g.

bismuth) growing via particle-mediated processes, such as orientated attachment [23]. Furthermore, anhydrite mesocrystals, specifically, were also found to be a byproduct of the bacterial dehydration of gypsum under very dry conditions [46], where particle-mediated nucleation is also suggested as the reason behind its mesocrystallinity.

In our earlier work we also showed that the re-structuring processes within the amorphous aggregates do not continue until a near-perfectly homogeneous single crystal is obtained, but instead it comes to a halt during the observation window, because any mass transport processes inside such aggregates must be subject to slow diffusional processes compared to those associated with ion transport through the bulk aqueous solution. This early-stage crystallization most likely leads to the formation of several-micron-sized single-crystalline seeds, which are followed by an (ultra-)slow "classical" ion-by-ion addition growth phase under thermodynamic conditions close to equilibrium. During such secondary ion-by-ion growth, the original non-classical mesostructured single crystals would constitute the aforementioned "seeds of imperfection". The consequent ion-by-ion growth is actually well-understood from the *in situ* atomic force microscopy measurements by Pina [47] and Morales et al. [48]. These studies demonstrate that when the anhydrite surface is in contact with a supersaturated solution, growth takes place at monolayer steps and the rate of step propagation increases rapidly with increasing supersaturation. At low supersaturation levels (β_{anh} < 2) monomolecular growth steps originate mainly at screw dislocations, whereas nucleation of monolayer 2D islands only occurs at β_{anh} > 2, but with very low nucleation densities (~1 nucleus/μm^2). Hence, 2D nucleation is not an effective growth mechanism for anhydrite at temperatures of up to 120 °C, and the screw dislocations are the dominant source of new steps. However, steps emanating from spiral hillocks undergo a structure-induced growth self-inhibition process [49] and for spiral growth to be efficient on the anhydrite surface, a high density of active screw dislocations is required. Hydrothermal AFM experiments also provided data on the growth kinetics of anhydrite[48]. As in the case of gypsum, the kinetic rate constant increases with temperature, but the absolute values are up to two orders of magnitude lower. The activation energy for step advancement was estimated to be 73 ± 5 kJ/mol, which is comparable to the value reported for the (0 1 0) face of gypsum (70 ± 5 kJ/mol, [50]) and only slightly higher than face-averaged activation energies extracted from gypsum bulk growth experiments. This indicates that the dehydration of ions, or other growth units/precursors, – and not ion incorporation – is the limiting factor for anhydrite growth from aqueous solution. This notion is corroborated by the observation that anhydrite can only be obtained at room temperature from liquid media containing very low amounts of water [51,52], which should facilitate this dehydration step. Overall, based on these studies we can conclude that the ion-by-ion growth of anhydrite is painstakingly slow. Moreover, from such a growth should render near perfect crystals.

However, this last sentence has to be rephrased to: such growth should "reproduce" near-perfectly the preexisting, i.e. underlying, crystalline matrix. We can envisage a situation that for the mesostructured crystal the inherent slight disorder in the crystalline matrix will be replicated through the length-scales. The as-growing crystallographic domains will eventually reach sizes of many microns, and what constituted a small misalignment at the scale of 10-20 nm, will be expressed as a microstructural

imperfection such as the complex void topology, which we observe in microtomography. The scattering behaviour that we see in SAXS can also be explained by the presence of voids, but at the length-scale of ~100 nm. Tilt-dependent SAXS patterns actually correspond to structural features, which could very well look exactly like those in µCT, if it was not for the fact that CT probes length scales > 500 nm, whereas SAXS in our configuration is limited to << 500 nm, where the largest structures (> 70 nm) could only be partially observed, if at all. This implies that the void topology extends to significantly smaller length-scales than those measured with µCT, in a self-similar manner. This is fully confirmed by our AFM images (Fig. 5), which demonstrate that the voids can be <100 nm, with an average size of 85 nm. Although AFM is essentially restricted to the external facets of the crystal, one can assume that the observed surface porosity extends into the third dimension, i.e. the surface pores should have their confined analogs within the volume of the crystal. In the context of the discussion above it is also worth considering, whether the observed voids might simply constitute dissolution etch pits [53], observed for many single crystals [54,55]. However, there are significant differences. Most importantly, our voids extend into the volume of the crystal whereas etch pits are typically limited to surfaces of crystals. Further deepening of etch pits leads to the formation of inverse pyramid dissolution patterns [53,54] and not vertical wells as those observed in our anhydrite samples. Moreover, etch pits should be filled up again when the crystal surface continues to grow, so it is highly unlikely that remnants of a large number of etch pits are preserved within the bulk of the crystal.

HRTEM revealed orientated amorphous/disordered regions, whose presence can be correlated with the diffuse scattering streaks observed in SAED and WAXS. In this regard, SAXS is likely to produce structural features from both voids and the disordered nano-sized regions, since they would all exhibit lower electron density than the crystalline anhydrite matrix, and therefore contribute to the scattering contrast. Hence, it is possible that the disordered part of the anhydrite mesocrystal is not reproduced at longer length-scales during the ion-by-ion growth, and instead voids are formed. The orientated and anisotropic character of the voids indicates, in this context, that they form as semi-regular errors in the replication/growth processes in a similar way as the order-disorder modulation is regular and anisotropic. Such a behaviour also explains the presence of the orientation-dependent small-angle diffraction peaks.

Finally, the EBSD results bridge our interpretation of the scattering data with what we observe in microtomography and other methods. This technique accesses the intermediate length-scales of several tens to several hundreds of nanometers, and highlights a heterogenous crystallographic character of the single crystal. Hence, the original "seed of imperfection" is expressed through the length-scales both in morphological (i.e. voids) as well as strictly structural (i.e. crystallographic) aspects of the actual single crystal.

Outlook and Conclusions

Ongoing investigations into the nucleation of various mineral systems seem to insinuate that non-classical pathways are much more common than was considered a decade or

two ago. In fact, it is even possible that some materials can nucleate both classically and non-classically, a phenomenon that was recently demonstrated for calcium oxalate [56]. Here, we show that the intrinsic mesocrystallinity, seen in both gypsum [8], and anhydrite [8,46], is imprinted evidence of non-classical, particle-mediated nucleation. This nucleation mechanism introduces a "seed(s) of imperfection", which still leads to a macroscopic single crystal, but in which its fragments do not fit together at different length-scales in a self-similar manner. This results in the formation of anisotropic voids of various sizes and with very well-defined walls/edges. This resembles nature playing a game of Tetris, which in some ways it is losing.

Materials and Methods

Anhydrite single crystals

Macroscopic well-formed translucent anhydrite samples were obtained from the Naica mine, Chihuahua, Mexico (municipality of Saucillo, the mine is owned by Industrias Peñoles). This mining area is located on the northern side of the Sierra de Naica [57], and constitutes one of the main lead and silver deposits in the world. Hydrothermal fluid circulation associated with Tertiary dikes formed these Ag-Pb-Zn deposits[58]. During the late hydrothermal stage sulfuric acid formed by oxidation of the underlying sulfides and reacted with the available limestone to form calcium-sulfate–rich waters that eventually precipitated anhydrite masses[21]. These specimens (Figs. S2 and S3) are famous for their high purity, light blue color and large size (single crystals can easily reach >10 cm). Almost all the experiments were performed on the same selected single crystal shard shown in SI: Fig. S3, which was chipped off from a bigger body of crystals similar to the one shown in SI: Fig. S2. The only exception was in the case of the atomic force microscopy characterisation (AFM, see below), for which we used another pristine shard from the same group.

Single Crystal X-ray Diffraction

Single crystal X-ray diffraction experiments were performed on a Bruker D8 Venture system with graphite-monochromatic Mo-Kα radiation (λ = 0.71073 Å). For the diffraction experiments the crystal (SI: Fig. S3) was not modified in any way, to ensure sample preservation for further analyses. Data reduction was performed with Bruker AXS SAINT[59] and SADABS[60] packages. The structure was solved in the space group Cmcm using direct methods and completed using differential Fourier maps calculated with SHELXL 2018[61]. Full matrix least-squares refinements were performed on F^2 using SHELXL 2018[61] with anisotropic displacement parameters for all atoms. All programs were run under the WinGX (v. 1.80) system[62]. VESTA (v. 3.5.7) was used for structure visualization[63]. The resulting crystal information file (CIF) is included as a part of the SI (anhydrite.cif). Diffraction unequivocally confirmed the single-crystalline character of the investigated anhydrite sample.

Scattering Methods

Small- and wide-angle X-ray scattering (SAXS/WAXS) measurements were conducted using the MOUSE instrument (a heavily modified Xenoxs XEUSS 2.0). X-rays were generated from a microfocus X-ray tube, followed by multilayer optics to parallelize and to monochromatise the X-ray beams to wavelength of Mo Kα (λ = 0.71073 Å). Scattered

radiation was detected on an in-vacuum Eiger 1M detector (Dectris, Switzerland), which was placed at multiple distances between 52 - 2354 mm from the sample. Beam parameters were kept consistent for all sample-to-detector distances used with a spot size of 643 μm (fwhm).

The anhydrite single crystal was placed on a goniometer for data collection to allow multiple orientations to be probed in SAXS and WAXS (SI: Fig. S3). The initial crystal orientation was arbitrary, and the goniometer was set to null positions. This starting orientation with a XZ-tilt of 0° constituted position S (SI: Fig. S3A). WAXS was measured starting from S, and at further positions N-W-E, 90° apart from each other, corresponding to a rotation of the crystal around its axis in the XY plane (SI: Fig. S3B). For SAXS, the crystal was returned to S (SI: Fig. S3A), and measured in a second step in position S with an additional XZ-tilt of 21° (SI: Fig. S3C).

The resulting data was processed using the DAWN software package (v. 2.20) in a standardized complete 2D correction pipeline with uncertainty propagation[64,65]. These included, among other steps, essential corrections for sample transmission and the instrument background subtraction. For SAXS, in order to compare the intensities in different directions the 2D patterns were also converted to polar coordinates ("cake" plots). Such a representation allows for an easy integration of the direction dependent-scattering intensities to 1D scattering curves. The azimuthal positions of the intensity directions of interest, as well as their angular widths are directly obtained from the mean intensity profiles.

In the case of WAXS, such a polar representation was the only one used, due to the fact that version 2.20 of DAWN applies a small-angle approximation to scale the Q_x- and Q_y-axis in 2D patterns. This issue does not affect SAXS, but at higher scattering angles the resulting scales are incorrect for 2D images in Cartesian coordinates. However, the small-angle approximation is not utilised for calculating the "cake" plots, hence they are rendered correctly for all angular ranges. In those cases when 2D WAXS in Cartesian coordinates were required, we back-calculated them from the "cake" plots rather than use outputs from DAWN, so that Q_x and Q_y were expressed correctly. Further processing and analysis of reduced 2D scattering datasets was performed in Python using NumPy, SciPy and Pandas[66–69]. The dataset is deposited at Zenodo[70].

Transmission Electron Microscopy

In order to analyse single crystals under a transmission electron microscope (TEM), we prepared ~15 μm x 4 μm thin foils (~100 nm thickness) using the focused ion beam technique (FIB, FEI FIB200) following a standard procedure [31,32]. Neither did the crystal show any signs of alteration under the vacuum of the instrument during cutting/milling, nor did the foils when imaged in TEM.

For TEM imaging and selected-area electron diffraction (SAED), a Tecnai F20 XTWIN TEM was used at 200 kV, equipped with a field-emission gun electron source. SAED patterns were collected using an aperture with an effective diameter of ~1 μm and the diffraction plates were developed in a high-dynamic range Ditabis Micron scanner. To correctly interpret any preferred orientation or texture-related effects in the TEM images, the objective stigmatism of the electron beam was corrected by ensuring the fast Fourier transform (FFT) was circular over the amorphous carbon film.

X-ray Microtomography

Microtomography (μCT) was performed with an EASYTOM (RX Solutions) equipped with a LaB$_6$ filament. The final resolution was set to 0.55 μm obtained by applying a voltage of 100 kV and a current of 100 μA and by collecting 2816 sinograms over a 360° rotation. With these settings, the collection time was set to ~38 h. 3D reconstruction was performed by the software provided by the manufacturer (RX Solutions). The collected 2816 sinograms were reconstructed using the Back Projection Algorithm into a 3D tomogram, where the YZ plane was 1447 x 1718 pixels^2, and the YX plane was 1447 x 1716 pixels^2. The reconstructed tomogram constituted raw data, which were processed by reslicing the dataset into the XY and XZ planes. For quantitative analysis, the 3D data was further processed by applying artifact correction and data restoration algorithms and scripts described in refs. [71–73]. The images in the XY plane revealed typical ring artifacts from the reconstruction processes, which were partially suppressed following the referenced method [71]. In the next step, the images were corrected for an illumination drift using histogram matching through the Z axis in the stack. A median filter with a 3-pixel 2D kernel together with a non-local means filter to suppress noise were applied which was necessary to perform feature analysis, because the rings and noise were hindering the deduction of the solid-void threshold parameter. Such as-calculated images were trimmed in order to remove the edge/background parts of the slices leaving only the measured crystal. We calculated gradients distribution of features that measured along which axes the defects were dominant, to see if the defects exhibited any anisotropy. This was performed separately for the XY and YZ plane because of the memory limitations, and demonstrated that the features were strongly anisotropic. Finally, an ellipse fit on the features was performed to further characterize their dimensions, which showed features were longer than wider. This was also readily visible from a visual inspection of the 3D projections. An example of uncorrected and corrected images is shown in SI: Fig. S6. The dataset and the uncompressed Videos S1-S3 are deposited at Zenodo[70].

Electron Backscatter Diffraction (EBSD)
We used electron backscatter diffraction (EBSD) in a scanning electron microscope (SEM)To characterize the general orientation and the intracrystalline distortion of the studied anhydrite single crystal. This was done on a FEI Quanta200 F SEM with EDAX EBSD/EDS detectors and Team/OIM Analysis software. The orientation map was collected from one of the single crystal facets, which exhibited very high apparent smoothness, and hence did not require any special sample preparation. The crystal was orientated in the vacuum chamber in a way that the elongated direction of the single crystal (~Z in SI: Fig. S3) was horizontal in the EBSD orientation maps and in the pole figures. The SEM operating conditions included an accelerating voltage of 20 kV, beam current of 8 nA, working distance of 15 mm and a step size of 100 nm, in an uncoated sample, with the SEM working under low vacuum (30 Pa H$_2$O). Post-acquisition processing included confidence index (CI) standardization with a grain tolerance angle of 5°, followed by one iteration of CI neighbour correlation considering only grains with CI >0.1. Afterwards, we removed all the pixels with CI <0.2 and image quality below 25% to ensure that the orientations presented here were correct. From the orientation map, we then calculated the kernel average misorientation (KAM) map calculated in relation to a fixed distance between neighbours, which showed the average misorientation of a given pixel in the map in comparison to all its neighbours. The as-obtained map had a threshold misorientation angle of 2.5° and was calculated in relation to the 1st neighbour

pixel. The crystal orientation data was plotted in the upper hemisphere of an equal-angle stereographic projection (SI: Fig. S7). Here, we plotted the three main crystal directions of anhydrite ([1 0 0],[0 1 0] and [0 0 1]) plus the direction <5 8 6>, which had one of the 4 symmetrically equivalent directions ([5 8 6],[-5 -8 6],[-5 8 -6] and [5 -8 -6]) plotted right in the middle of the pole figure and thus indicate which crystal direction is approximately normal to the reader when looking at the orientation map. That indicated that this direction was normal to the facet, which was equivalent to a crystal plane within the {9 5 3} group ((9 5 3), (-9 -5 3), (-9 5 -3) or (9 -5 -3)).

Atomic Force Microscopy
Topographical features of the studied anhydrite sample (see also Methods: Anhydrite single crystals*)* were evaluated using Atomic Force Microscopy (AFM) operating in contact mode using a MFP-3D microscope from Asylum Research (Santa Barbara, USA). The maximum range of the piezo scanner is 120 μm in the planar direction (XY) and 15 μm in the vertical direction (Z). All the AFM images were acquired by using triangular silicon nitride cantilevers (PNP-TR from NanoWorld) with a nominal spring constant of 0.08 $N·m^{-1}$. Before each experiment the used cantilever was routinely calibrated using the thermal method. All the obtained images were processed using the AR and WSxM softwares [74]. Images collected at a field-of-view length-scale of ~120 μm were post-processed by applying a thresholding algorithm that filtered out all topographical features above 20 nm (set as a threshold value). As a result, filtered AFM images were obtained showing almost exclusively the pores/voids, which allowed us to perform quantitative calculations of the volume, surface and perimeter of the pores.

References
1. Gebauer, D., Völkel, A. & Cölfen, H. Stable prenucleation calcium carbonate clusters.

    Science **322**, 1819–1822 (2008).

2. De Yoreo, J. J. *et al.* Crystallization by particle attachment in synthetic, biogenic, and

    geologic environments. *Science* **349**, aaa6760 (2015).

3. Van Driessche, A. E. S., Kellermeier, M., Benning, L. G. & Gebauer, D. *New*

    Perspectives on Mineral Nucleation and Growth: From Solution Precursors to Solid

    Materials. (Springer, 2017).

4. Gilbert, P. U. P. A. *et al.* Biomineralization by particle attachment in early animals. *Proc.*

Natl. Acad. Sci. **116**, 17659–17665 (2019).

5. Stawski, T. M. *et al.* Formation of calcium sulfate through the aggregation of sub-3 nanometre primary species. *Nat. Commun.* **7**, 11177 (2016).

6. Stawski, T. M. *et al.* Nucleation Pathway of Calcium Sulfate Hemihydrate (Bassanite) from Solution: Implications for Calcium Sulfates on Mars. *J. Phys. Chem. C* **124**, 8411–8422 (2020).

7. Van Driessche, A. E. S., Stawski, T. M. & Kellermeier, M. Calcium sulfate precipitation pathways in natural and engineered environments. *Chem. Geol.* **530**, 119274 (2019).

8. Stawski, T. M. *et al.* Particle-Mediated Nucleation Pathways Are Imprinted in the Internal Structure of Calcium Sulfate Single Crystals. *Cryst. Growth Des.* **19**, 3714–3721 (2019).

9. Cölfen, H. & Antonietti, M. *Mesocrystals and Nonclassical Crystallization: New Self-assembled Structures*. (Wiley, 2008).

10. Ma, M.-G. & Cölfen, H. Mesocrystals — Applications and potential. *Curr. Opin. Colloid Interface Sci.* **19**, 56–65 (2014).

11. Niederberger, M. & Cölfen, H. Oriented attachment and mesocrystals: non-classical crystallization mechanisms based on nanoparticle assembly. *Phys. Chem. Chem. Phys.* **8**, 3271–3287 (2006).

12. Van Driessche, A. E. S., Garcia-Ruiz, J. M., Tsukamoto, K., Patino-Lopez, L. D. & Satoh, H. Ultraslow growth rates of giant gypsum crystals. *Proc. Natl. Acad. Sci.* **108**, 15721–15726 (2011).

13. Freyer, D. & Voigt, W. Crystallization and phase stability of CaSO4 and CaSO4–based salts. *Monatshefte Für ChemieChemical Mon.* **134**, 693–719 (2003).

14. Schmid, T., Jungnickel, R. & Dariz, P. Insights into the CaSO4–H2O System: A Raman-Spectroscopic Study. *Minerals* **10**, 115 (2020).

15. Christensen, A. N., Olesen, M., Cerenius, Y. & Jensen, T. R. Formation and Transformation of Five Different Phases in the CaSO 4 −H 2 O System: Crystal

Structure of the Subhydrate β-CaSO 4 ·0.5H 2 O and Soluble Anhydrite CaSO 4. *Chem. Mater.* **20**, 2124–2132 (2008).

16. Cruft, E. F. & Chao, P.-C. Nucleation kinetics of the gypsum-anhydrite system. in *IO9-118. 3rd Symp. on salt* vol. 1 (1970).

17. Sharpe, R. & Cork, G. Gypsum and anhydrite. *Ind. Miner. Rocks Commod. Mark. Uses* (2006).

18. Ossorio, M., Van Driessche, A. E. S., Pérez, P. & García-Ruiz, J. M. The gypsum–anhydrite paradox revisited. *Chem. Geol.* **386**, 16–21 (2014).

19. García-Ruiz, J. M., Villasuso, R., Ayora, C., Canals, A. & Otálora, F. Formation of natural gypsum megacrystals in Naica, Mexico. *Geology* **35**, 327–330 (2007).

20. Foshag, W. F. The selenite caves of Naica, Mexico. *Am. Mineral.* **12**, 252–256 (1927).

21. Stone, J. G. Ore genesis in the Naica District, Chihuahua, Mexico. *Econ. Geol.* **54**, 1002–1034 (1959).

22. Zhu, G. *et al.* Self-similar mesocrystals form via interface-driven nucleation and assembly. *Nature* **590**, 416–422 (2021).

23. Li, J. *et al.* In Situ Atomic-Scale Study of Particle-Mediated Nucleation and Growth in Amorphous Bismuth to Nanocrystal Phase Transformation. *Adv. Sci.* **5**, 1700992 (2018).

24. You, H. & Fang, J. Particle-mediated nucleation and growth of solution-synthesized metal nanocrystals: A new story beyond the LaMer curve. *Nano Today* **11**, 145–167 (2016).

25. Welberry, T. R. & Weber, T. One hundred years of diffuse scattering. *Crystallogr. Rev.* **22**, 2–78 (2016).

26. Chapman, B. D. *et al.* Diffuse x-ray scattering in perovskite ferroelectrics. *Phys. Rev. B* **71**, 020102 (2005).

27. Bosak, A. *et al.* Short-Range Correlations in Magnetite above the Verwey Temperature. *Phys. Rev. X* **4**, 011040 (2014).

28. Bosak, A., Chernyshov, D., Vakhrushev, S. & Krisch, M. A new model of correlated disorder in relaxor ferroelectrics. *arXiv:1101.0490 [cond-mat]* http://arxiv.org/abs/1101.0490 (2011).

29. Kwei, G. H., Lawson, A. C., Billinge, S. J. L. & Cheong, S. W. Structures of the ferroelectric phases of barium titanate. *J. Phys. Chem.* **97**, 2368–2377 (1993).

30. Egami, T. & Billinge, S. J. *Underneath the Bragg peaks: structural analysis of complex materials*. (Elsevier, 2003).

31. Wirth, R. Focused Ion Beam (FIB) combined with SEM and TEM: Advanced analytical tools for studies of chemical composition, microstructure and crystal structure in geomaterials on a nanometre scale. *Chem. Geol.* **261**, 217–229 (2009).

32. Wirth, R. Focused Ion Beam (FIB): A novel technology for advanced application of micro- and nanoanalysis in geosciences and applied mineralogy. *Eur. J. Mineral.* **16**, 863–876 (2004).

33. Huh, Y., Hong, K. J. & Shin, K. S. Amorphization Induced by Focused Ion Beam Milling in Metallic and Electronic Materials. *Microsc. Microanal.* **19**, 33–37 (2013).

34. Kato, N. I. Reducing focused ion beam damage to transmission electron microscopy samples. *J. Electron Microsc. (Tokyo)* **53**, 451–458 (2004).

35. Porod, G. Die Abhängigkeit der Röntgenkleinwinkelstreuung von Form und Grösse der Kolloiden Teilchen in verdünnten Systemen, IV. *Acta Phys. Austriaca* **2**, 255–292 (1948).

36. Wong, P. & Bray, A. Porod scattering from fractal surfaces. *Phys. Rev. Lett.* **60**, 1344 (1988).

37. Besselink, R., Stawski, T. M., Van Driessche, A. E. S. & Benning, L. G. Not just fractal surfaces, but surface fractal aggregates: Derivation of the expression for the structure factor and its applications. *J. Chem. Phys.* **145**, 211908 (2016).

38. Stawski, T. M. *et al.* The Structure of CaSO4 Nanorods: The Precursor of Gypsum. *J. Phys. Chem. C* **123**, 23151–23158 (2019).

39. Wang, Y.-W., Kim, Y.-Y., Christenson, H. K. & Meldrum, F. C. A new precipitation pathway for calcium sulfate dihydrate (gypsum) via amorphous and hemihydrate intermediates. *Chem. Commun.* **48**, 504–506 (2012).

40. Wang, Y.-W. & Meldrum, F. C. Additives stabilize calcium sulfate hemihydrate (bassanite) in solution. *J. Mater. Chem.* **22**, 22055–22062 (2012).

41. Stach, R., Krebs, P., Jones, F. & Mizaikoff, B. Observing non-classical crystallisation processes in gypsum via infrared attenuated total reflectance spectroscopy. *CrystEngComm* **19**, 14–17 (2017).

42. Jones, F. Infrared investigation of barite and gypsum crystallization: Evidence for an amorphous to crystalline transition. *CrystEngComm* **14**, 8374–8381 (2012).

43. Jia, C. *et al.* Structural Characteristics of Amorphous Calcium Sulfate: Evidence to the Role of Water Molecules. *J. Phys. Chem. C* **125**, 3415–3420 (2021).

44. Li, H.-J. *et al.* Structures and dynamic hydration of CaSO4 clusters in supersaturated solutions: A molecular dynamics simulation study. *J. Mol. Liq.* **324**, 115104 (2021).

45. Zhang, Q.-W. *et al.* Effects of methanol on CaSO4 ion associated species in mixed solutions: Solvation dynamics and hydrogen bond bridging structure. *J. Mol. Liq.* **307**, 112985 (2020).

46. Huang, W. *et al.* Mechanism of water extraction from gypsum rock by desert colonizing microorganisms. *Proc. Natl. Acad. Sci.* **117**, 10681–10687 (2020).

47. Pina, C. M. Nanoscale dissolution and growth on anhydrite cleavage faces. *Geochim. Cosmochim. Acta* **73**, 7034–7044 (2009).

48. Morales, J., Astilleros, J. M. & Fernández-Díaz, L. A nanoscopic approach to the kinetics of anhydrite (100) surface growth in the range of temperatures between 60 and 120 °C. *Am. Mineral.* **97**, 995–998 (2012).

49. Pina, C. M., Becker, U., Risthaus, P., Bosbach, D. & Putnis, A. Molecular-scale mechanisms of crystal growth in barite. *Nature* **395**, 483–486 (1998).

50. Van Driessche, A. E. S. *et al.* In situ observation of step dynamics on gypsum crystals. *Cryst. Growth Des.* **10**, 3909–3916 (2010).

51. Tritschler, U., Van Driessche, A. E. S., Kempter, A., Kellermeier, M. & Cölfen, H. Controlling the selective formation of calcium sulfate polymorphs at room temperature. *Angew. Chem. - Int. Ed.* **54**, 4083–4086 (2015).

52. Tritschler, U., Kellermeier, M., Debus, C., Kempter, A. & Cölfen, H. A simple strategy for the synthesis of well-defined bassanite nanorods. *CrystEngComm* **17**, 3772–3776 (2015).

53. Dove, P. M., Han, N. & De Yoreo, J. J. Mechanisms of classical crystal growth theory explain quartz and silicate dissolution behavior. *Proc. Natl. Acad. Sci.* **102**, 15357–15362 (2005).

54. Qin, L., Putnis, C. V. & Wang, L. Facet-Specific Dissolution–Precipitation at Struvite–Water Interfaces. *Cryst. Growth Des.* (2021) doi:10.1021/acs.cgd.1c00400.

55. Visconti, P. *et al.* Dislocation density in GaN determined by photoelectrochemical and hot-wet etching. *Appl. Phys. Lett.* **77**, 3532–3534 (2000).

56. Banner, D. J. *et al.* In Situ Liquid-Cell TEM Observation of Multiphase Classical and Nonclassical Nucleation of Calcium Oxalate. *Adv. Funct. Mater.* **31**, 2007736.

57. Naica, Saucillo Municipality, Chihuahua, Mexico. https://www.mindat.org/loc-2308.html.

58. Megaw, P. K. M., Ruiz, J. & Titley, S. R. High-temperature, carbonate-hosted Ag-Pb-Zn(Cu) deposits of northern Mexico. *Econ. Geol.* **83**, 1856–1885 (1988).

59. Sheldrick, G. M. A short history of SHELX. *Acta Crystallogr. A* **64**, 112–122 (2008).

60. Sheldrick, G. M. SADABS, Empirical Absorption Correction Program; University of Göttingen: Göttingen, Germany, 1997. *Google Sch. There No Corresp. Rec. This Ref.* (2002).

61. Sheldrick, G. M. SHELXT – Integrated space-group and crystal-structure determination. *Acta Crystallogr. Sect. Found. Adv.* **71**, 3–8 (2015).

62. Farrugia, L. J. WinGX suite for small-molecule single-crystal crystallography. *J. Appl. Crystallogr.* **32**, 837–838 (1999).

63. Momma, K. & Izumi, F. VESTA 3 for three-dimensional visualization of crystal, volumetric and morphology data. *J. Appl. Crystallogr.* **44**, 1272–1276 (2011).

64. Basham, M. *et al.* Data Analysis WorkbeNch (DAWN). *J Synchrotron Rad* **22**, 853–858 (2015).

65. Pauw, B. R., Smith, A. J., Snow, T., Terrill, N. J. & Thünemann, A. F. The modular small-angle X-ray scattering data correction sequence. *J. Appl. Crystallogr.* **50**, 1800–1811 (2017).

66. Oliphant, T. E. *Guide to NumPy*. vol. 1 (2006).

67. Virtanen, P. *et al.* SciPy 1.0: fundamental algorithms for scientific computing in Python. *Nat. Methods* **17**, 261–272 (2020).

68. McKinney, W. Data Structures for Statistical Computing in Python. *Proc. 9th Python Sci. Conf.* 56–61 (2010) doi:10.25080/Majora-92bf1922-00a.

69. Reback, J. *et al. pandas-dev/pandas: Pandas 1.3.0rc1*. (Zenodo, 2021). doi:10.5281/zenodo.4940217.

70. Stawski, T. M. *et al.* Supplementary Data Set for 'Seeds of imperfection rule - Mesocrystalline disorder in natural anhydrite single crystals'. (2021) doi:10.5281/zenodo.4943234.

71. Jha, D., Sørensen, H. O., Dobberschütz, S., Feidenhans'l, R. & Stipp, S. L. S. Adaptive center determination for effective suppression of ring artifacts in tomography images. *Appl. Phys. Lett.* **105**, 143107 (2014).

72. Szczepanowska, H. M., Jha, D. & Mathia, T. G. Morphology and characterization of Dematiaceous fungi on a cellulose paper substrate using synchrotron X-ray microtomography, scanning electron microscopy and confocal laser scanning microscopy in the context of cultural heritage. *J. Anal. At. Spectrom.* **30**, 651–657

(2015).

73. Přikryl, J., Jha, D., Stefánsson, A. & Stipp, S. Mineral dissolution in porous media: An experimental and modeling study on kinetics, porosity and surface area evolution. *Appl. Geochem.* **87**, 57–70 (2017).

74. Horcas, I. *et al.* WSXM: A software for scanning probe microscopy and a tool for nanotechnology. *Rev. Sci. Instrum.* **78**, 013705 (2007).

75. Rueden, C. T. *et al.* ImageJ2: ImageJ for the next generation of scientific image data. *BMC Bioinformatics* **18**, 529 (2017).

76. Anhydrite. *mindat.org* https://www.mindat.org/photo-261625.html.

77. Schrank, C. E. *et al.* Tracking Metamorphic Dehydration Reactions in Real Time with Transmission Small- and Wide-Angle Synchrotron X-ray Scattering: the Case of Gypsum Dehydration. *J. Petrol.* **61**, egaa041 (2020).

Figures

Fig. 1. HRTEM analysis of a FIB foil from the anhydrite single crystal; A) and B) show two similar HRTEM images of the small sections of the foil, which are >10 µm apart from each other. Inset I in (A), and II in (B) show FFTs calculated to the respective images; selected reflections in FFTs are indexed for anhydrite; flux: ~8x10^5 e$^-$Å^{-2}s^{-1}, estimated received fluence ~1x10^{27} e$^-$m^{-2}; Pink rectangles in (A) and (B) correspond to the same regions-of-interest (ROIs) in (C) and (D), respectively; C) Inverse FFT and filtered image, which highlights the order-disorder in (A) with a fake-colour palette applied; light-blue lines trace the lattice fringes in two directions; inset III shows 2x magnified overlap between the ROIs marked by the pink rectangles, so that the light-blue lines remain continuous; the arrows point to an apparent lattice fringe shift (*pseudo*-dislocation) along the selected light-blue line; D) Inverse FFT and filtered image, which highlights the order-disorder in (B) with a fake-colour palette applied; inset IV shows the ROI contained in a pink rectangle and 3x magnified; the arrows in IV point to highly-disordered/amorphous regions in the crystal.
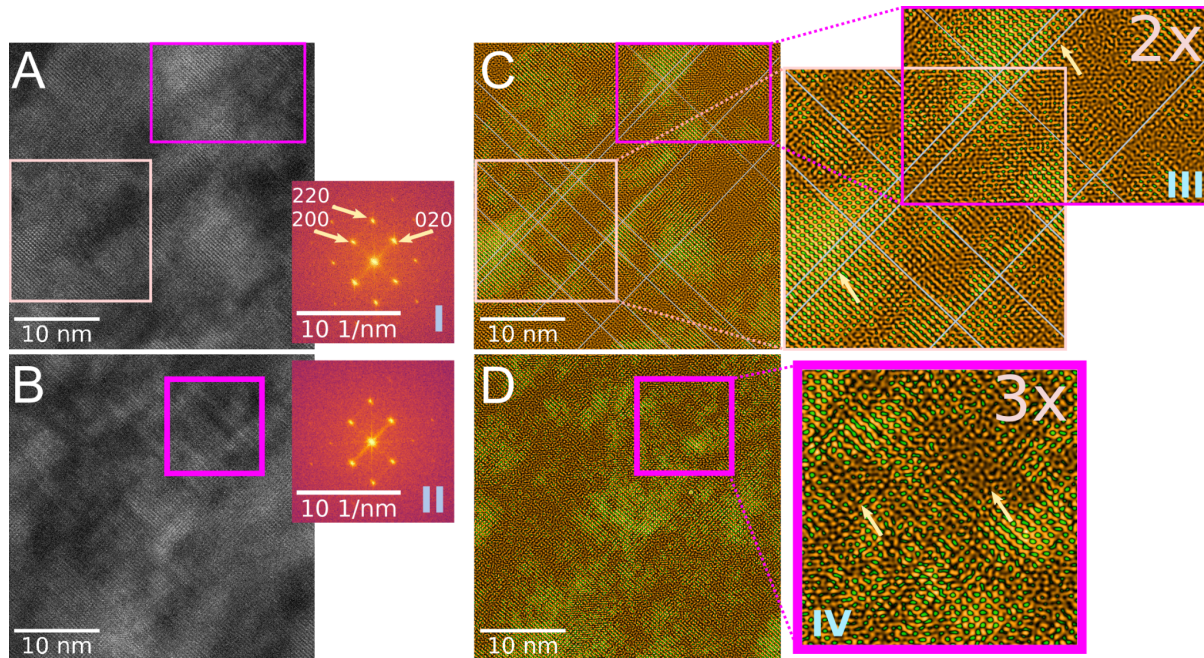
Fig. 2. SAXS scattering patterns from the anhydrite crystal. A) 2D SAXS (left) pattern of the anhydrite crystal in Position S at 0° (see also SI: Fig. S3A); B) 2D SAXS (left) pattern of the

anhydrite crystal in Position S at 21° tilt (see also SI: Fig. S3C); In (A) and (B) The angular directions marked with dotted lines indicate integration directions based on the polar coordinate representations shown in SI: Fig. S5; C) and D) Direction-dependent scattering curves integrated from (A) and (B) respectively (see also SI: Fig. S7). Fitted scattering dependencies in a form of $I(Q) \propto Q^{-a}$, where $-a$ is a scattering exponent, are indicated with dotted red lines; the Porod-scattering (smooth interface) $I(Q) \propto Q^{-4}$ is shown with dashed black lines; C) Position S at 0°, averaged high-intensity direction (black), and low-intensity direction (purple); curves are obtained by integrating intensity profiles with centroids of azimuthal angles as written in the legends, and based on (A) and II in SI: Fig. S5A; each of two symmetric profiles are averaged together; D) Position S at 21° tilt; three characteristic scattering directions are shown I (orange), II (cyan and purple), III (black); curves are obtained by integrating intensity profiles with centroids of azimuthal angles as written in the legends, and based on (B) and II in SI: Fig. S5B.
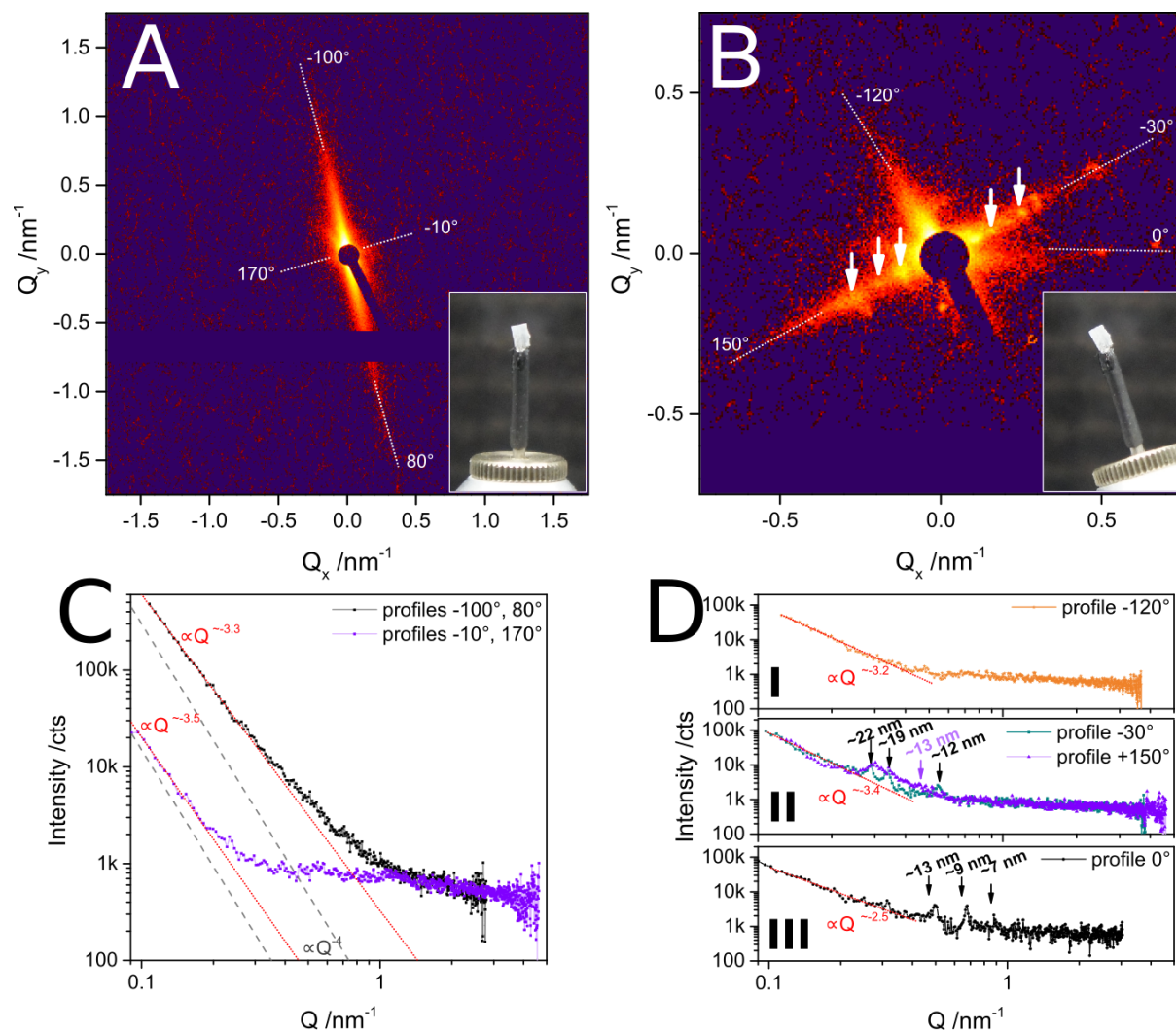
Fig. 3. WAXS diffraction/scattering patterns from the anhydrite crystal. A) Composite WAXS 2D diffraction pattern, which consists of four panels. The data are plotted in polar

coordinates (the "cake plot"). The diffraction patterns were measured for four orientations resulting from a rotation of a crystal around the goniometer's vertical axis, Z, where consecutive panels correspond to positions in Fig. 1B: I (starting), II (180° clockwise), III (90° clockwise), IV (270° clockwise). Furthermore, each of the panels comprises five sub-patterns obtained by moving the detector in a plane perpendicular to the beam i.e. emulating a larger area detector. For the overlapping pixels among such sub-patterns the intensities were averaged out. The discussed peaks at $Q \sim 28$ nm^{-1} are indicated with arrows; the cross-shaped reflection is marked with a dashed rectangle; B) close-up 2D WAXS in polar coordinates, and profile plots of the reflection marked in (A); an arrow points to a diffuse scattering streak; C) 2D WAXS in Cartesian coordinates of the two peaks at $Q \sim$ 28 nm^{-1} from the 1st panel in (A); the diffuse scattering streaks are well-pronounced; the Cartesian-coordinates representation is re-calculated from the polar coordinates.
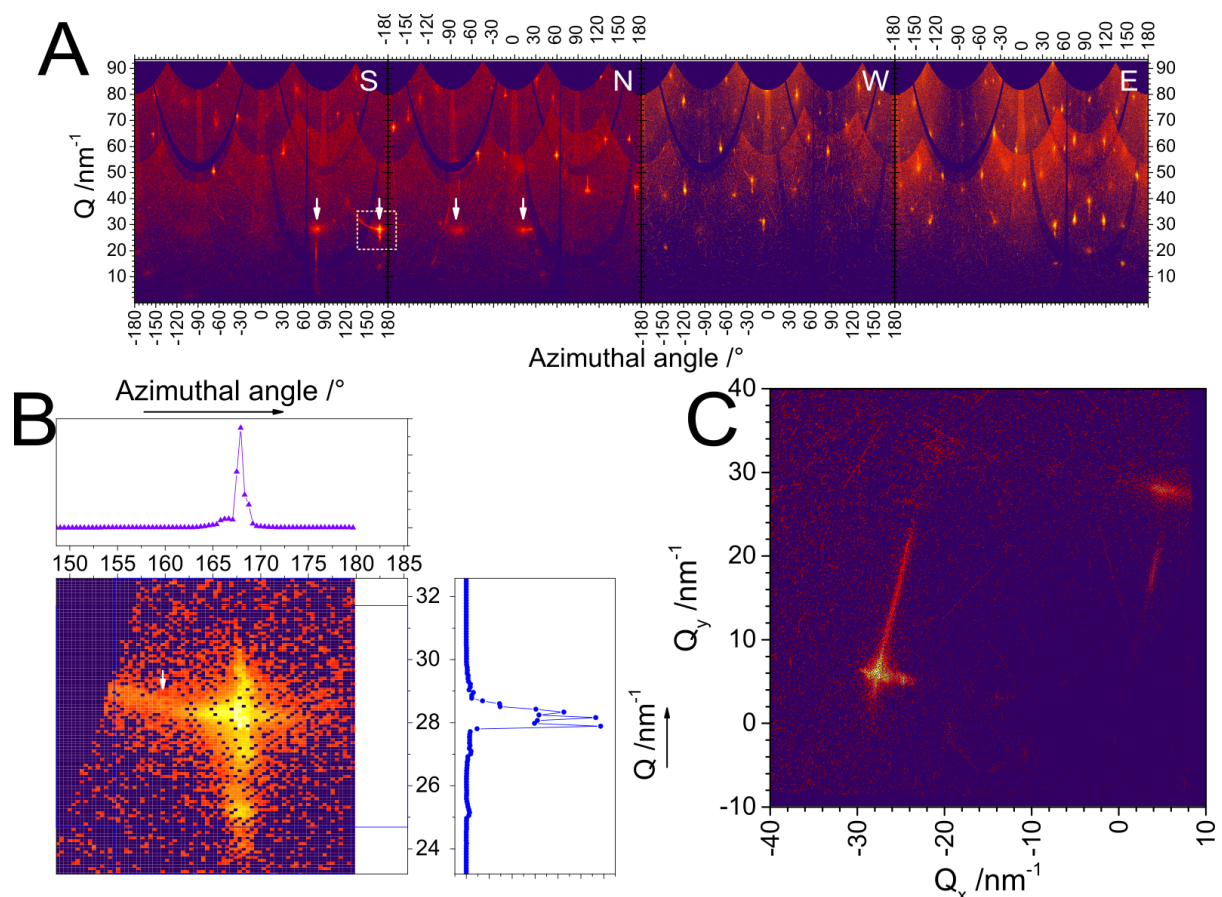
Fig. 4. Microtomographic reconstructions and analysis. A) Selected projections from a 3D reconstruction of an uncorrected (see Methods) microtomography data set collected for the anhydrite single crystal; the projections show the two sides of the crystal (left and right) and

highlight internal defect structure; see also SI: Video S1 - overview 360° rotation in the XY-plane around Z, and SI: Video S2 - overview 360° rotation in the XZ-plane around Y; B) Selected processed (see Methods) cross-sections in the XY plane for two arbitrary Z-values; the voids are shown in blue; an inset graph on the left shows the overall abruptness of the contrast transition between the void and the surrounding crystal matrix; the co-centric rings are a typical artifact of the reconstruction processes, and in the image they are already partially suppressed (see Methods); C) a projection of a segmentation which shows the void structure within the crystal, derived from the processed data such as those in (B); see also SI: Video S3 - 360° rotation in the XY-plane around Z which highlights the void structure; D) distribution of voids' dimensions in XY- and ZY-planes calculated from the corrected data, which demonstrates the anisotropic character of the defects; E) distribution of voids' orientations in XY- and ZY-planes calculated from the corrected data, which demonstrates the preferred orientation of the defects along Z and Y.

A

500 µm

500 µm

Z   Z

X   X

B   Z = 370.15 µm

X
Y

Z = 618.20 µm

Intensity /a.u.
160
120
80

0 40 80
Distance /µm

200 µm

200 µm

C

200 µm

Z

Y   X

D

0.16
0.14
0.12
0.10
0.08
0.06
0.04
0.02
0.00

Relative Frequency

length
width

XY

0.30

0.20

0.10

0.00

length
width

ZY

5 10 15 20

5 10 15 20

Size /µm

E

XY
ZY

0.6
0.5
0.4
0.3
0.2
0.1
0.0

0 15 30 45 60 75 90

Angle /°
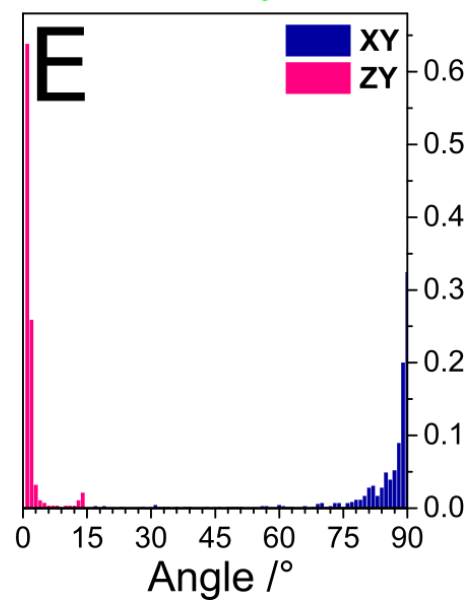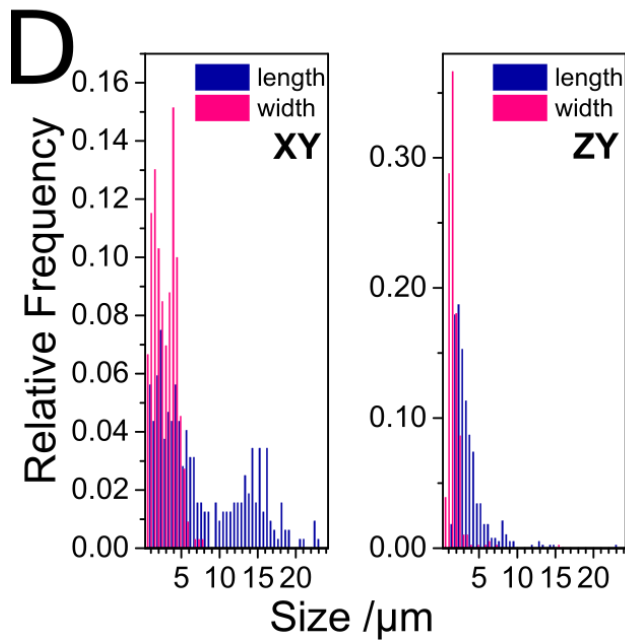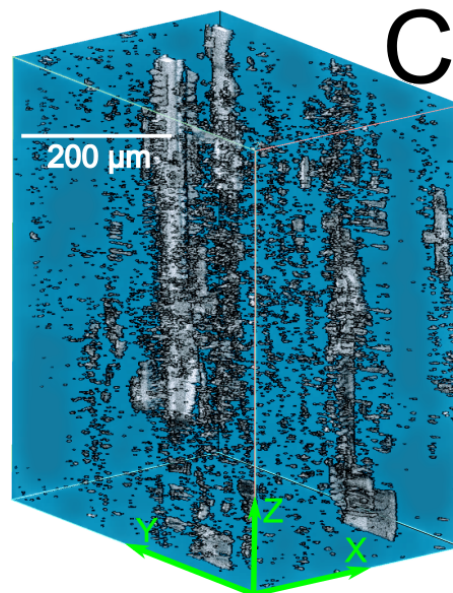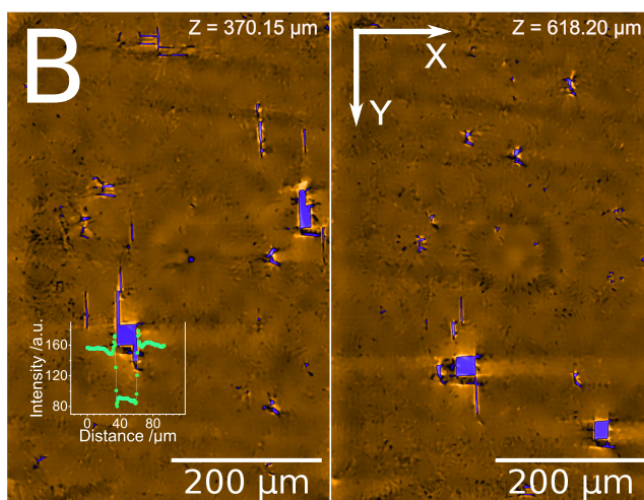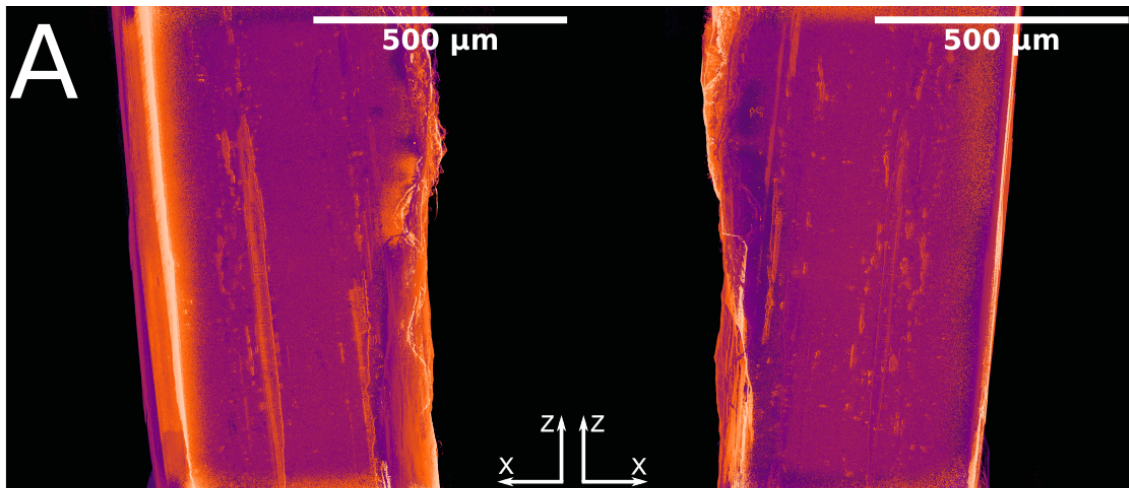
Fig. 5. AFM characterisation of the crystal facets. A) View of a typical hydrothermal anhydrite sample from Naica; a side of the black square, on which the crystal is laid, is 1 cm. AFM images of the selected sides of the anhydrite crystal, which show topographical details of B) the top face at low magnification; C) the top face at high magnification; D) the side face at low magnification. The smallest observed voids exhibit well-defined edges and are <100 nm in size. E) the pore/void size distribution on the anhydrite surface obtained from the quantitative analysis of the AFM topographical images; F) the pore/void size distribution at the nanometre-length scale, where a maximum can be observed at ~85 nm; an average void size is calculated as (length+width)/2.
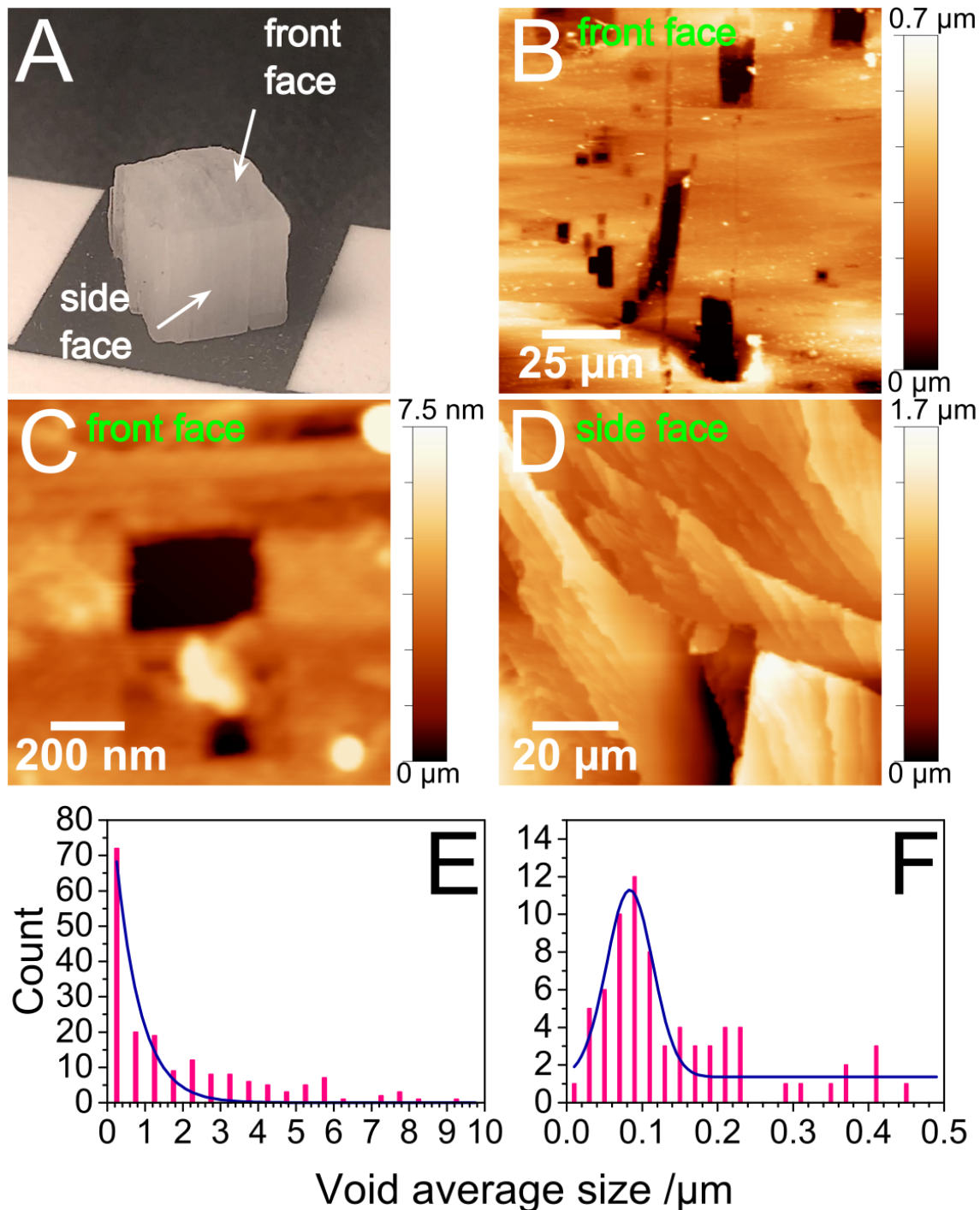
Fig. 6. EBSD maps of the selected crystal facet. A) Orientation map from the (9 5 6) facet parallel to Z in SI: Fig. S3. The corresponding pole figure is shown in SI: Fig. S7. The total viewed area is 51 x 51 µm^2 at a resolution of 100 nm. A *quasi*-uniform cyan colour indicates that the studied sample is a single crystal; B) Kernel average misorientation (KAM) map for the 1st neighbours with a 2.5° threshold, which highlights a heterogeneous character of (A); C) A cropped image from (B) which further illustrates the intrinsic disorder down to ~100 nm; D) distribution of orientations in (B) for the complete area (black), the upper half of the image (pink) and the lower half of the image (blue); in (B) and (C) the intensity is expressed using a Green-Fire-Blue palette (black-blue-green-yellow) from ImageJ2[75] , where green codes misorientation of ~ 0.9° and black of 0°.
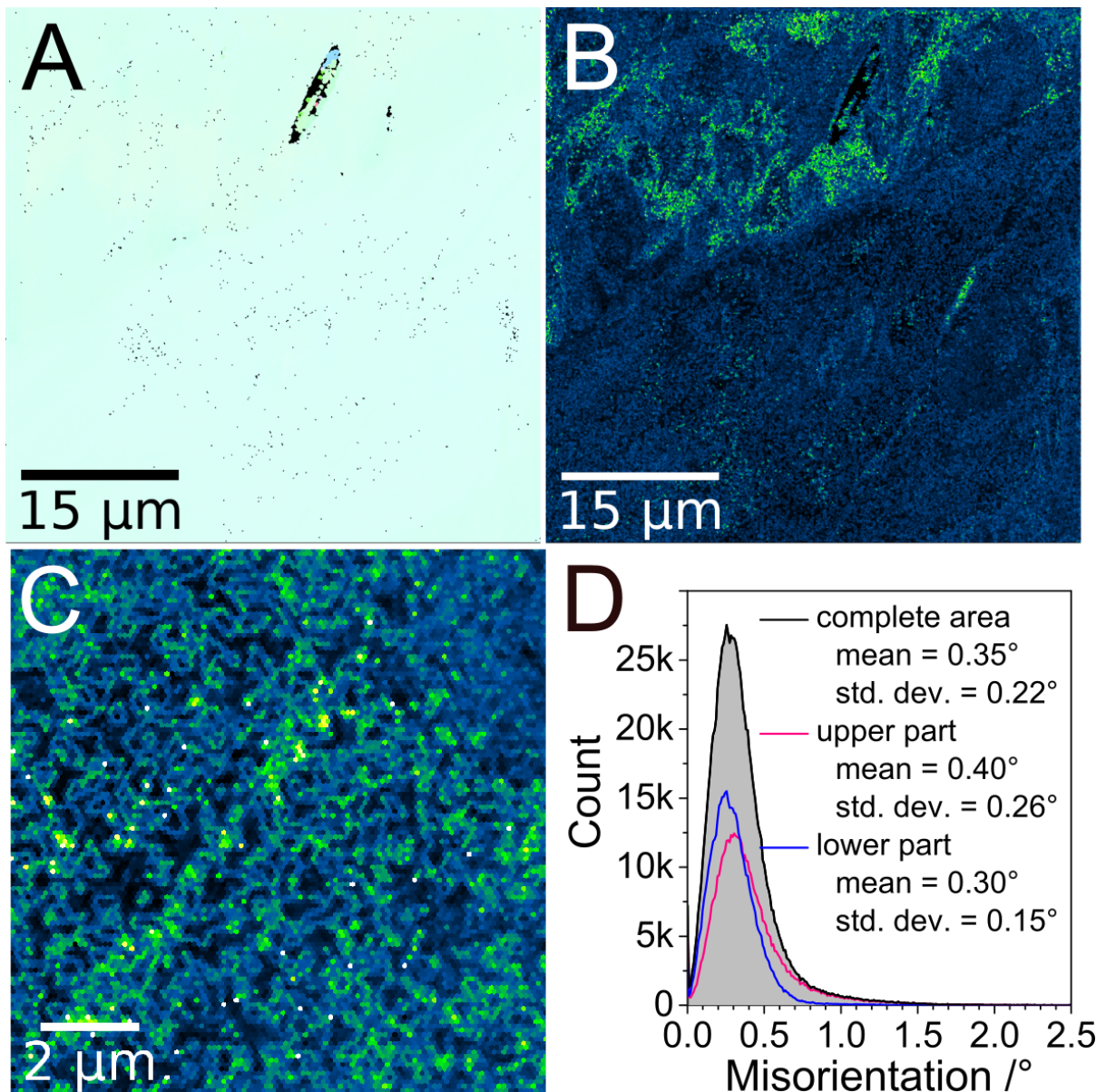
Supplementary Information for:

Seeds of imperfection rule the
mesocrystalline disorder in natural anhydrite single crystals

Tomasz M. Stawski*, Glen J. Smales, Ernesto Scoppola, Diwaker Jha, Luiz F. G. Morales,
Alicia Moya, Richard Wirth, Brian R. Pauw, Franziska Emmerling,
and Alexander E. S. Van Driessche**

* tomasz.stawski@bam.de; **Alexander.Van-Driessche@univ-grenoble-alpes.fr

Table of Contents:

Supplementary Figures

Fig. S1. Visualisation of different crystal structures of $CaSO_4$; Blue spheres - Ca^{2+}, yellow-red stick tetrahedra - SO_4^{2-}, red spheres - O in H_2O; The crystal orientations/projections are expressed by three vectors *a* - red, *b* - green, *c* - blue; A) $CaSO_4 \cdot 2H_2O$, gypsum; B) $CaSO_4 \cdot 0.5H_2O$, bassanite; C) γ-$CaSO_4$, AIII anhydrite; D) β-$CaSO_4$, AII insoluble anhydrite. Prepared in VESTA[63].

Fig. S2. Centimetric hydrothermal anhydrite single crystals from the Naica Mine, Mexico. Specimen size is 16.8 cm x 15.4 cm x 10.8 cm, and the largest anhydrite "fans" are up to 10.5 cm long[76]. (R.M. Lavinsky, CC-BY-SA-3.0)
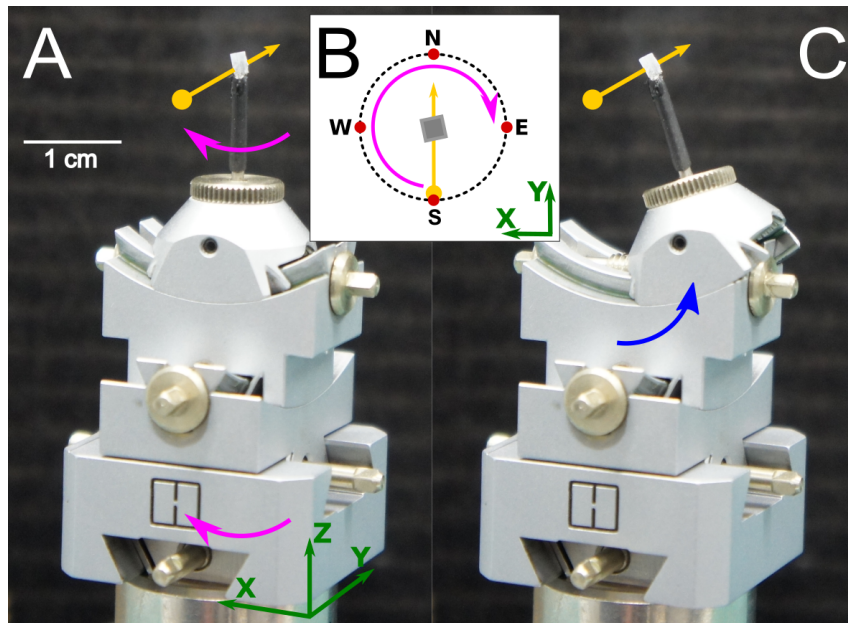
Fig. S3. Anhydrite crystal orientations during WAXS and SAXS measurements. The initial crystal orientation was arbitrary, and the goniometer was set to null positions. The XYZ cardinal directions are indicated in green; the X-ray beam direction is marked with a yellow arrow, where the beam is parallel to Y; the magenta arrow indicates the direction of rotation in the XY plane; the blue arrow indicates a tilt direction in XZ plane; A) Initial crystal orientation, I, used for the WAXS and SAXS measurements; XZ-tilt was 0°; B) Further crystal positions I-IV, 90° apart from each other, used only for WAXS corresponding to a rotation of the crystal around its axis in the XY plane; C) Crystal in position I with an additional XZ-tilt of 21° used for SAXS.

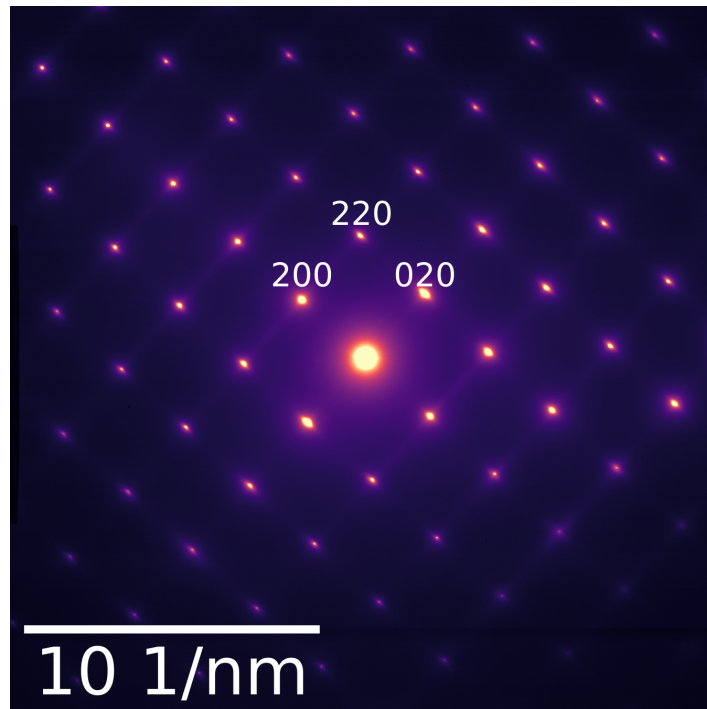Fig. S4. SAED pattern from a FIB foil, which corresponds to a field of view of 2 μm x 2 μm, and measured with a 1 μm aperture. Characteristic reflections of anhydrite are indexed. Diffuse scattering streaks are visible. They are parallel to 100 (weaker) and 010 (stronger) directions, and passing through all diffraction spots.
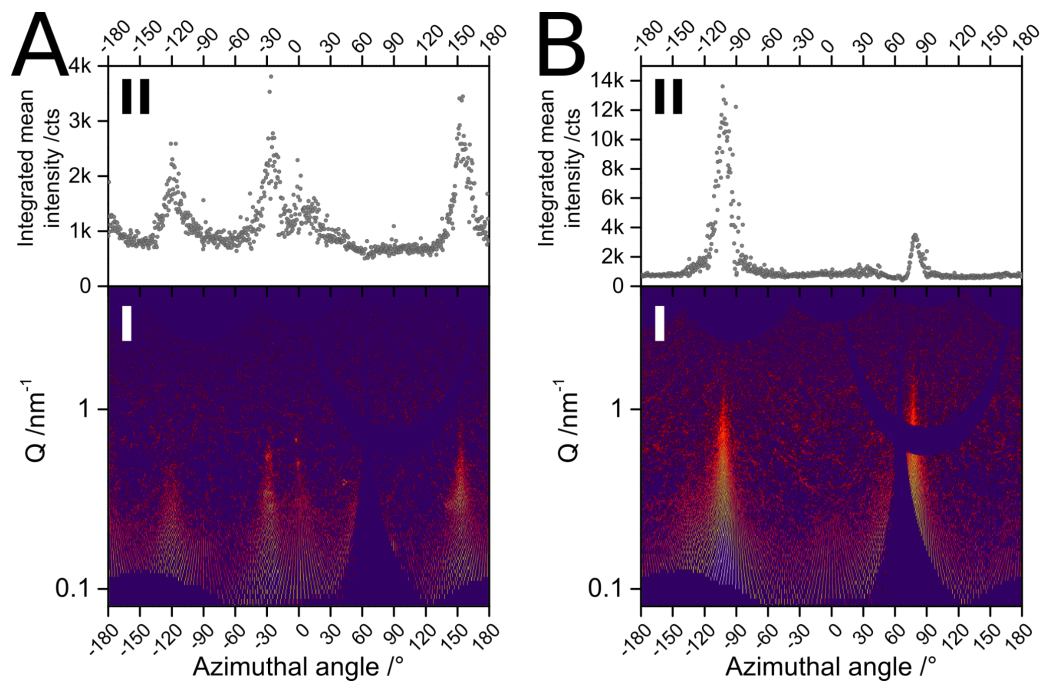

Fig. S5. Polar-coordinate representation of the SAXS data in Fig. 2 in the main text, where a cake plot is in I, and the integrated mean intensity from I is plotted in II. A) Transformed SAXS from Fig. 2A of the crystal in Position S at 0°; B) Transformed SAXS from Fig. 2B of the crystal in Position S at 21° tilt.
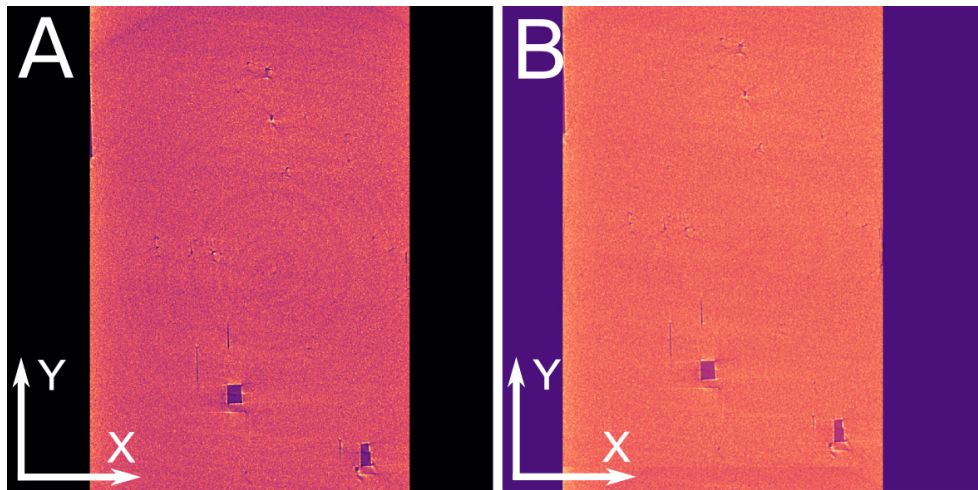
Fig. S6. An example of reconstructed images in the XY-plane from our tomography dataset, before (A) and after (B) corrections following ref.[71]. In (A) the artifactual reconstruction co-centric rings are clearly visible, whereas in (B) they are considerably suppressed, although still present.
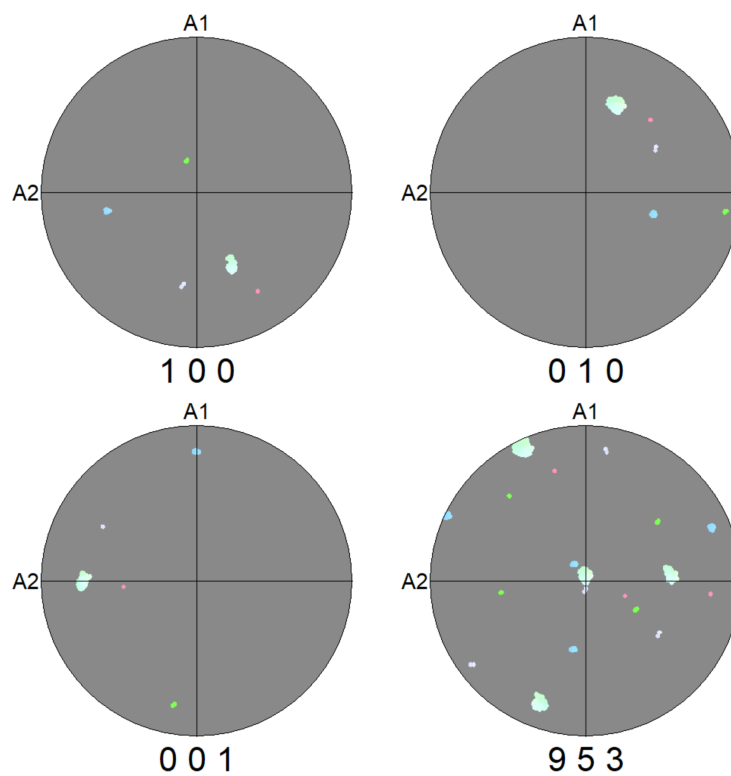

Fig. S7. Pole figures of the crystal orientation data plotted in the upper hemisphere of an equal-angle stereographic projection with the three main crystal directions of anhydrite ([1 0 0],[0 1 0], [0 0 1]) and the poles to (9 5 3), one of which plots right in the middle of the pole figure and indicate that the mapped facet is parallel to this anhydrite crystal plane).

Supplementary Notes

Supplementary Note 1: Anhydrite and other phases of CaSO$_4$

Anhydrite is one of the three major phases of calcium sulfate. Its geological name directly implies that it is anhydrous (CaSO$_4$) in contrast to dihydrate gypsum (CaSO$_4$.2H$_2$O) and hemihydrate bassanite (CaSO$_4$.0.5H$_2$O). In terms of crystallography and physicochemical properties anhydrite at least three major (sub)phases ought to be considered designated as AI, AII and AIII. They differ in terms of structure, stability, formation pathway and natural occurrence. In the conceptually easiest case, anhydrite is formed in the course of dehydration of gypsum by heat treatment under wet and/or dry conditions. For the temperatures upto ~200 °C, gypsum converts first to bassanite: an alpha-form for dry calcination in air, and a beta-form for heating in water, aqueous solutions, organic solvents e.g. alcohols or in the presence of water vapour[7]. The structural differences between the α- and β- hemihydrates are rather minor (although present) and appear to be more relevant at a morphological level. In general, the layered structure of gypsum (with alternating water and CaSO$_4$ in parallel sheets, Fig. S1A) is converted into a distinct channel structure of bassanite (Fig. S1B). The channels are formed by CaSO$_4$ chains aligned along the *c*-axis, and are filled with water molecules. Upon prolonged and slow exposure to high temperatures (upto ~200 ºC) water is lost gradually, which converts bassanite to an AIII anhydrite (γ-CaSO$_4$) phase. AIII anhydrite is crystallographically distinct from bassanite, but the two compounds are closely related, and often difficult to unequivocally recognise by diffraction methods[15]. In bassanite, along the *c*-axis direction parallel to the channel (Fig. S1B), a channel is formed/surrounded by three Ca^{2+} ions and three sulfate tetrahedra arranged into an imperfect hexagonal pattern, while in AIII anhydrite an analogous hexagonal arrangement appears perfectly ordered (Fig. S1C). Importantly, AIII anhydrite is metastable and will react with even trace amounts of water, and convert back to bassanite through, as it appears, a simple crystal lattice rearrangement. Therefore, the AIII phase is also known as soluble anhydrite, and is found practically only in engineered environments. In this regard, the further rehydration of bassanite back to gypsum is far more complex as it occurs through a dissolution-reprecipitation crystallisation mechanism (ref). An ongoing heat-treatment beyond ~200, and upto 1200 °C, converts the metastable AIII form into an orthorhombic AII phase (insoluble anhydrite, β-CaSO$_4$), which has either two or three pseudo-phases depending on the actual calcination temperature (Fig. S1D). These sub-phases are crystallographically identical and the differences are morphological, which still affects e.g. reactivity with water. In air AII is stable up to 1200 °C and in water AII is the thermodynamic stable form from[7,13] ~42-58 °C also up to 1200 °C, above which a high-temperature AI form is found[14,15] (α-CaSO$_4$). As it is explained in the main text, anhydrite AII is commonly encountered in evaporitic environments on the Earth's surface and it is also the only natural anhydrite phase (at least on Earth), which can crystallise directly from aqueous solutions. Hence, a natural AII anhydrite phase can be obtained through two non-related pathways/mechanisms: high-temperature calcination[14,77] or aqueous crystallisation[18]. Although the final material is identical in terms of the molecular structure, at the microstructural level the resulting solid phases are clearly different in terms of morphology, crystallite size and habit etc. In particular, a slow growth from aqueous solution

may potentially yield macroscopic single crystals of AII anhydrite, which are not conceivable in the course of thermal treatment of hydrated calcium sulfate phases.

Supplementary Note 2: Scattering from idealised single crystals
Here, we first consider how an idealised macroscopic single crystal, i.e. infinitely large and continuous from the point of probed length-scales, should scatter both in the SAXS and WAXS range. Typically for a crystal of a simple inorganic compound one would expect that at decreasing scattering angles in SAXS, the probed characteristic distances increase, and thus at the mesoscale the considered single crystal would appear to be a homogenous and a continuous object in terms of electron density contrast. Effectively, SAXS should yield a featureless flat signal, *i.e.* $I(q) \propto q^0$, proportional to the square of the electron density of the material. Moreover, such a SAXS pattern would be isotropic and independent from the crystal orientation. Mesoscale and atomic-scale defects in the crystal structure, such as point defects, dislocations or stacking faults, at the length-scales probed by SAXS would not contribute sufficiently to electron density contrast variations in the material. On the other hand, for the considered case WAXS directly should correspond to a typical single crystal diffraction measurement, in which sharp diffraction spots are observed. The intensity and the position/arrangement of single spots would depend on the actual structure and symmetry, as well as on the relative crystal orientation with respect to the beam and the detector. Thus, in general the recorded scattering signal should be anisotropic in WAXS.

Supplementary Note 3: Analysis of direction-dependent SAXS profiles
In Fig. 2A in the main text, two regions are considered: (1) a high-intensity profile with a centroid at -100° together with its symmetric counterpart at +80° integrated for azimuthal angles ±22.5°, and (2) a low-intensity profile at -10° and 170° integrated in the same way. The two resulting curves are shown in Fig. 2C. In comparison, the cross-shaped scattering pattern in Fig. 2B contains more direction-dependent components. Based on representation II in Fig. 2B, the first high-intensity direction has a centroid at -120°, but its symmetric counterpart at +60° is nearly fully covered by the beamstop. The resulting integrated curve I is shown Fig. 2D. The second high-intensity direction has a pair of centroids at -30° and +150° i.e. perpendicular to the 1st direction. In this case the two curves (II in Fig. 2D) were not averaged together to highlight better the weak small-angle diffraction peaks, which are stronger for the +150° centroid side. In addition, the pattern in Fig. 2B shows a narrow streak at ~30° diagonally from the main cross-shaped pattern at 0°. This streak nominally should also have a +180° counterpart, but it is less pronounced and noisy, and hence was not included in the integration to a final curve III in Fig. 2D. The observed slight asymmetries in the complementary scattering profiles most likely stem from sample thickness variations and hence different absorption values across the sample.